RSC Advances

PAPER

View Article Online
View Journal | View Issue

Cite this: *RSC Adv.*, 2020, **10**, 37374

Converting cellulose nanocrystals into photocatalysts by functionalisation with titanium dioxide nanorods and gold nanocrystals†

Santhosh S. Nair,‡ Jianhong Chen,‡ Adam Slabon * and Aji P. Mathew *

Received 8th July 2020
Accepted 21st September 2020

DOI: 10.1039/d0ra05961g

rsc.li/rsc-advances

Cellulose nanocrystals (CNCs) are promising building blocks for water purification due to their high surface area, tuneability of surface charge and grafting of surface groups depending on the pollutants. In this report we have converted CNCs into photocatalysts, without altering the surface groups, by *in situ* growth of TiO_2 nanorods (NRs) and functionalization with Au nanocrystals (NCs) for enhanced light absorption. The control of the density of the NRs assures that the CNC surface and functionalities are accessible for the pollutant, followed by the photocatalytic degradation on the light absorption layer under solar illumination. This seed-mediated NR synthesis can be applied to realize a series of CNC-inorganic NR photocatalysts. The low temperature (90 °C compared to commonly reported growth at 150 °C) of the NR growth provides the opportunity to use nanostructured biopolymers as functional substrates for preparation of photocatalysts using a bio-inspired design.

Introduction

Hybrid bio-inorganic nanostructures are promising materials for energy and environmental applications while simultaneously enabling environment-friendly degradation pathways toward a circular economy.[3] Nanocellulose in the form of cellulose nanocrystals (CNCs) or cellulose nanofibers (CNFs) is considered as a prospective functional material owing to the abundance and renewability of its source and its versatile surface chemistry. For example, CNCs with sulphonyl or carboxylic acid functionality show high uptake capacities for cationic dyes such as methylene blue, malachite green and basic fuchsin,[4,5] whereas amino-functionalized CNCs show a high uptake of anionic dyes.[6] Thus, water treatment is an emerging application for nanocellulose,[1,2] but suffers still from limitations related to reusability.

Nanostructured cellulose acts as a universal substrate for growth of different nanocrystals (NCs),[7] which offers the opportunities toward the design of hybrid materials including semiconductors. Nanostructures of the latter play the leading role in applications covering adsorption, energy conversion, electronics, gas sensors and catalysis.[8–10] Recently, nanocellulose–TiO_2 interfaces have received attention to promote the removal of volatile organic compounds and arsenic in waste water through photocatalytic decomposition. Although TiO_2 can only absorb 4% of the solar light spectrum, it offers several advantages, such as high photocatalytic activity if sufficient light absorption is provided by the external source of illumination, chemical inertness, cost effectiveness, nontoxicity and long term stability against photocorrosion.[9,11,12] Contrariwise, cellulose as an insulating substrate can provide a mechanical support to NCs, minimize the aggregation of NCs, and the available functional groups of cellulose can interact with the pollutant.[13–17] In comparison to TiO_2 NC photocatalysts, one-dimensional nanostructures of TiO_2 offer the possibility to decouple the light absorption from charge carrier transport. The augmented charge carrier separation efficiency results in reduced electron–hole recombination.[18–20] Nanowires or nanorods can also scatter light due to the comparable size with the wavelength of visible light.[21] Therefore, TiO_2 NRs are considered as highly desired structures for photocatalytic applications, and have been demonstrated to exhibit high photocatalytic activity on mineralization of many organic and microbial contaminants under UV irradiation.[22,23] For example, Lv *et al.* has proved that TiO_2 nanowires have better photodegradation activity on methylene blue than TiO_2 nanotubes under UV irradiation.[24]

Department of Materials and Environmental Chemistry, Stockholm University, Svante Arrhenius väg 16C, SE-106 91, Stockholm, Sweden. E-mail: adam.slabon@mmk.su.se; aji.mathew@mmk.su.se; Tel: +46 8161236; +46 8161256

† Electronic supplementary information (ESI) available: ESI_CNCPhotocatalysts_Nair *et al.* Fig. S1. (a) AFM images of typical CNCs produced by sulphuric acid hydrolysis and (b–d) CNC/TiO_2-NRs hybrids based on sulphonyl, carboxyl and phosphoryl functionalized CNC nanocrystals; Fig. S2. TGA curves of the different functionalized CNCs (ramp 10 °C min^{-1}, 30–650 °C, in air); Fig. S3. TGA curves of the CNC/TiO_2-NRs(90) and CNC/TiO_2-NRs(150) (ramp 10 °C min^{-1}, 35–850 °C, in air); Fig. S4. Nitrogen adsorption–desorption BET isotherms of CNC/TiO_2-NRs(90) and CNC/TiO_2-NRs(150); Fig. S5. TEM image of Au NCs before decoration; Fig. S6. Tauc plot images of CNC/TiO_2-NRs(90), CNC/TiO_2-NRs(150), CNC/TiO_2-NRs(90)/Au NCs and CNC/TiO_2-NRs(150)/Au NCs; degradation mechanism while using solar simulator. See DOI: 10.1039/d0ra05961g

‡ Equal contributions from SSN and JC.

However, the wide electronic band gap of TiO_2 (3.0–3.2 eV) still confines the application of potential cellulose–TiO_2 hybrids to the UV region.[25,26] Surface decoration with plasmonic nanostructures is a potential way to extend the absorption towards the visible region.[27–29] Modification of the semiconductor surface with plasmonic Au and Ag NCs has shown a strong enhancement on photocatalytic activity in the visible region *via* the local surface plasmon resonance (LSPR).[30–33] The LSPR arises from collective oscillation of free electrons in the conduction band (CB) as a response to the electromagnetic field of incident light.[34] Meanwhile, the highly energetic electrons generated from the plasmon decay, described frequently as 'hot electrons', escape to the CB of semiconductors over the Schottky barrier and participate in the photocatalytic process.[35–39] As a result, the deposition of Au NCs on TiO_2 has become a promising interfacial structure for dye degradation in the longer wavelength region. Although the synthesis of cellulose–TiO_2 hybrids by impregnation of a Ti-precursor on cellulose and subsequent annealing is today established, precise control on the nanoscopic level has not been achieved so far. For the fabrication of hierarchical semiconductor nanostructures with well-defined semiconductor interfaces on cellulose, allowing to take advantage of suitable band alignment, it is a critical requirement to control the nucleation.

In this manuscript we report the successful use of cellulose nanocrystals as a functional template for the *in situ* growth of TiO_2 nanorods and subsequent decoration with Au nanocrystals and its application for the photocatalytic degradation of dyes under solar illumination. While nanocellulose–TiO_2 hybrids have been reported earlier, the growth of one dimensional TiO_2 on organic substrates is usually limited to highly thermally stable substrates such as FTO. Seed mediated synthesis for TiO_2 NRs on CNCs at 90 °C was developed by using a novel process and the synthesis was successful with different surface functional groups (sulphonic, carboxyl or phosphoryl) on cellulose nanocrystals (CNCs).

Experimental

Synthesis of CNC/TiO_2-NRs(90) and CNC/TiO_2-NRs(150)

Sulphonyl and phosphoryl functionalized CNCs were synthesized from microcrystalline cellulose using H_2SO_4/H_3PO_4 hydrolysis as reported in the previous literature (Fig. S1a†).[40,41] The carboxylic acid functionalized CNCs were extracted from bioethanol residue as reported.[42] Hence obtained CNC suspensions were freeze dried. 0.01 g of CNCs were ultrasonically dispersed in absolute ethanol (10 mL) in a capped bottle, and then stirred for 1 h to form a homogeneous suspension. Titanium butoxide (0.01 mL) was injected into the suspension, which was further stirred for 1 h and then the solution was allowed to age at 60 °C for 3 h. The suspension was filtered, dried and annealed at 100 °C to produce TiO_2 seeds on the CNCs. For synthesizing CNC/TiO_2-NRs(90), the seed deposited CNCs were dispersed in 10 mL of DI water and mixed with equal amount of conc. HCl and stirred for 1 h to get an homogeneous solution. Then 1 mL $TiCl_4$ solution was added and heated to 90 °C for 5 h with stirring. The obtained CNC/TiO_2-NRs(90) were filtered and washed with water, followed by ethanol to remove unreacted species and dried at vacuum at 60 °C for 12 h. Similar process was followed for CNCs with carboxyl and phosphoryl groups as well. Fig. S1b–d† shows that CNC–TiO_2 NRs can be prepared irrespective of the surface functionality of the CNC substrates. It has to be noted that there was no autoclave used in this method. The synthesis was carried out at ambient temperature and pressure to make it suitable for specific low temperature substrates, such as CNCs or other polymer substrates.

Different functionalized CNCs exhibit different thermal stabilities, hence more reliable carboxylic acid functionalized CNCs were used for the preparation of CNC/TiO_2-NRs(150), seed coated CNCs were ultrasonically dispersed in DI water (25 mL), mixed with conc. HCl (25 mL) and 1.0 mL of $Ti(OBu)_4$, and the resulting solution was placed in a 60 mL Teflon-lined autoclave. After stirring for 5 min, the autoclave was sealed and heated to 150 °C for 4 h and then allowed to cool to RT. The as-obtained product was washed successively with DI water and ethanol to remove any residual ionic species, and finally dried in vacuum at 60 °C for 12 h.

Preparation of CNC/TiO_2-NRs(90)/Au NCs and CNC/TiO_2-NRs(150)/Au NCs

The Au NCs were synthesized by colloidal method.[43] In detail, 20 mL of 1-octadecene (90%, Aldrich) was loaded in a three-neck flask and degassed with nitrogen at 130 °C for 30 min. After cooling down to room temperature, 1.316 mL (4 mmol) oleylamine (90%, Aldrich), 1 g (4 mmol) 1,2-hexadecanediol (90%, Aldrich) and 299.2 mg (0.8 mmol) anhydrous gold(III) acetate (99%, Alfa Aesar) were added into the flask. Then the temperature was increased to 200 °C under nitrogen flow for 2 h, after which the solution was cooled down again to room temperature. 35 mL ethanol (99.95%, Geyer Chemsolute GmbH) was added into the solution to precipitate the NCs and centrifuged at 12 000 rpm for 20 min. The Au NCs were redispersed in hexane after being washed once with ethanol. The composites CNC/TiO_2-NRs(90)/Au NCs and CNC/TiO_2-NRs(150)/Au NCs were fabricated by adding the respective CNC/TiO_2-NRs powder to a hexane dispersion of Au NCs. The mixture was sonicated for 5 min and dried under ambient atmosphere for 24 h.

Characterization

Thermal gravity analysis (TGA, Perkin Elmer TGA 7) measurement was used for the thermal properties of CNC/TiO_2-NRs(90) and CNC/TiO_2-NRs(150), the heating rate was 10 °C min^{-1} in air. Micromeritics ASAP 2020 instrument was used for nitrogen adsorption–desorption study, all samples were degassed at 90 °C for 5 h. For the Scanning electron microscopy (SEM) study on CNC/TiO_2-NRs(90) and CNC/TiO_2-NRs(150), the JEOL 7000F electron microscope with an accelerating voltage of 15 kV was used. X-ray diffraction (XRD) analysis is carried out using Panalytical X'Pert alpha1 with Cu-Kα1 line. Raman analysis is carried out using Horiba Labram HR 800 with 532 nm laser in the spectral range of 100–1000 nm. Transmission electron microscopy (TEM) images including high-resolution

transmission electron microscopy (HRTEM) images, selected area electron diffraction (SAED) and energy dispersive spectroscopy (EDS) as well as High-angle annular dark-field (HAADF) scanning transmission electron microscopy (STEM) micrograph were obtained by JEOL-2100F field emission transmission electron microscopy. The optical properties of different samples were studied using UV-vis spectrophotometer (Agilent Cary 5000) in the spectral range of 250–800 nm.

Photocatalytic experiments

The degradation rate of rhodamine B (RhB, pure, Acros) was employed to evaluate the photocatalytic performance of CNC/TiO_2-NRs(90)/Au NCs and CNC/TiO_2-NRs(150)/Au NCs and the hydrogen peroxide (35 wt%, ACROS) was used as electrons scavengers. The solution was illuminated with 100 mW cm^{-2} AM 1.5G light (1 sun) generated by a solar light simulator (class-AAA 94023A, Newport) with an ozone-free 450 W xenon short-arc lamp. For each experiment, 200 mg of sample was placed in 50 mL of aqueous solution of RhB (8 ppm). For every 20 min, an appropriate amount of solution was taken out and filtered to remove the solid catalyst particles, and the degradation rate of RhB in the solution was determined as a function of irradiation time using the intensity of the main absorbance band at the wavelength of 555 nm by UV-vis spectroscopy (WPA S800+, Biochrom).

Results and discussion

Seed-mediated synthesis at low temperature is known for binary metal oxides, such as ZnO and CuO, due to the availability of the nanoseed preparation methods which do not require high temperature annealing methods.[17] However for TiO_2, it is limited to the substrates which need to be annealed at 500 °C due to the lack of necessary and sufficient crystallinity/orientation in promoting one directional crystal growth. This is the main reason why previous reports were all conducted on highly thermally stable substrates such as FTO, carbon fibers *etc.*[44,45]

In this work, we demonstrate that CNCs can be used as a functional substrate to grow TiO_2 NRs and thus yield nanostructured hybrid biologic-inorganic NR photocatalysts which can be further decorated with Au NCs (Scheme 1). CNCs synthesized typically have a length of 200–300 nm and diameter of 5–10 nm with aspect ratio varying (20–60) as per AFM measurement (see Fig. S1a†).

The surface functionalities of CNCs can be tuned using different mineral acids. For example, H_2SO_4/H_3PO_4 can be used for hydrolysis to obtain sulphonyl and phosphonyl functionalized CNCs. The carboxyl functionalized CNCs has been extracted from bioethanol residue. The TGAs of different functionalized CNCs shows the varying degradation temperatures such as sulphonyl (180 °C), phosphonyl (204 °C) and carboxylic (240 °C) surface groups (see Fig. S2†) indicating that none of these materials can be annealed at 500 °C as reported in available reports.[44]

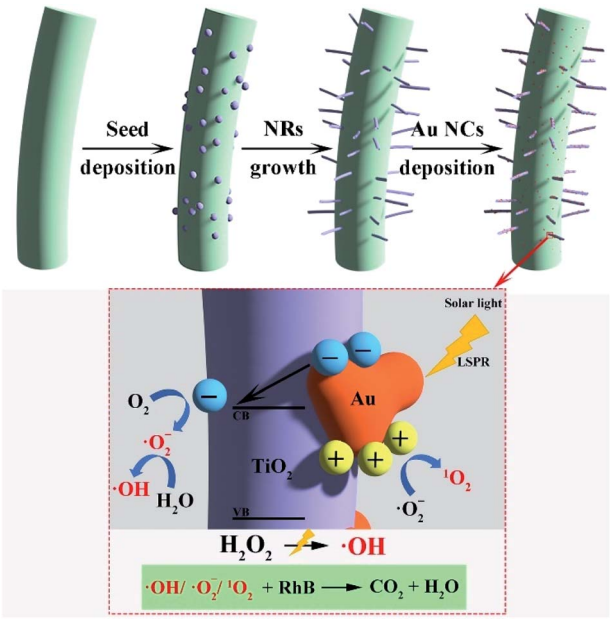

Scheme 1 Schematic representation of seed mediated TiO_2 NR synthesis, Au NCs deposition and suggested photocatalytic process for dye degradation.

We have synthesized TiO_2 seeds using sol–gel method with a slow hydrolysis of $Ti(OBu)_4$ in absolute ethanol and increased the crystallinity by aging at 60 °C. During sol–gel synthesis, the precursor used for hydrolysis and the conditions such as pH and temperature defines the phase of the nanoparticle formed. Increasing acidity and concentration of $TiCl_4$ as precursor forms generally rutile phase, however the usage of titanium alkoxide such as $Ti(OBu)_4$ at pH 7 at relatively low temperature forms the anatase phase.[44] During the hydrolysis, TiO_2 nanosheets are formed and subsequent aging results in their rolling-up to particle structures with a mean particle size of 30 nm. As shown in Fig. 1A, the SAED patterns indicate that the polycrystalline particles crystallize with mixed phases of predominately anatase-type structure containing typical reflections at (101), (200) (105), (220), (303) and (109). However, the signature reflections of rutile (210) is also present.

In the following step, we have exposed the seed coated CNCs in two different growth media, resulting in two different growth mechanisms. Low temperature growth has been carried out at 90 °C using equivalent amount of conc. HCl and water with 1 mL $TiCl_4$ as precursor. The formed TiO_2 NRs have an average length of (1.5 ± 0.23) μm and diameter of (48 ± 4) nm (Fig. 1B). It has been proved that in seed-mediated synthesis, the seed coated substrate has to be placed in the growth solution in particular way to ensure uniform growth in the desired and preferred crystal growth axis.[15] However, in our case, the TiO_2 nanoseeds have been coated on CNCs with the latter being in random motion inside the solution under stirring as evident by the birefringence (inset Fig. 1B and C). It should be noted that the latter is synthesized using autoclave method at the higher temperature, so it may adversely affect the surface functional groups on CNCs compared to CNC/TiO_2-NRs (90) and forms

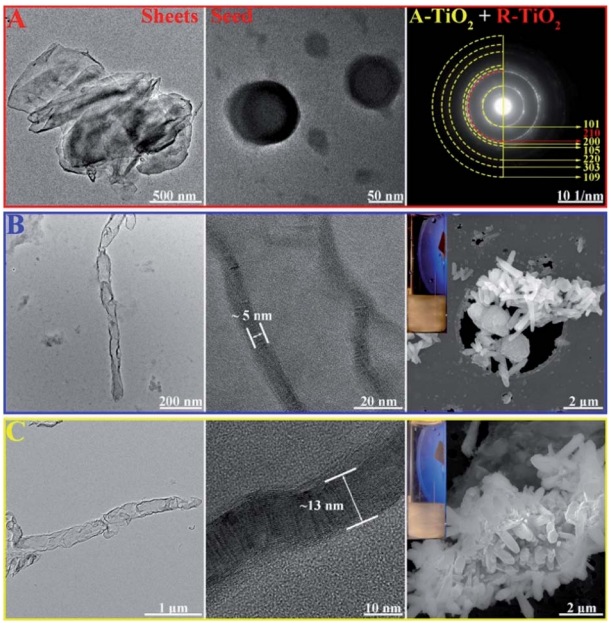

Fig. 1 TEM images of (A) TiO_2 nanosheets, nanoseeds and corresponding SAED pattern of TiO_2 nanoseeds, (B) TEM images of TiO_2-NRs(90) and HRTEM image of the walls of TiO_2 NRs (90), SEM images of CNC/TiO_2-NRs(90) and the flow birefringence of the hybrid (inset) (C) TEM image of TiO_2-NRs(150) and HRTEM image of boundary of TiO_2 NRs (150), SEM images of CNC/TiO_2-NRs(150) and the inset image showing the birefringence of the hybrids.

high aspect ratio nanorods. The thickness of the walls of the TiO_2 NRs synthesized at low temperature was found to be 4–5 nm (Fig. 1B). The high temperature synthesis was carried out hydrothermally in an autoclave using $Ti(OBu)_4$ as precursor as reported in the previous reports.[44] Thus, synthesized NRs had 250 nm diameter and >2 μm length (Fig. 1C). This is in contrast to previous reports showed equivalent amount conc. HCl and water with Ti precursor producing rutile phase NRs.[46]

One of the main parameters we have chosen for the optimization of the NR synthesis was well defined vertically grown (radially arranged on CNCs) NRs which is confirmed by SEM images (Fig. 1B and C). Birefringence, a characteristic property of anisotropic CNCs due to flow induced alignment, was retained in the hybrids (inset Fig. 1B and C) indicating that nano-properties of CNCs are maintained. It was noted that the growth without pre-seed deposition does not form NRs but rather formed a thick coating of TiO_2. The TGA analysis of the CNC/TiO_2-NRs(90) and CNC/TiO_2-NRs(150) was carried out in air. As shown in Fig. S2,† the CNC/TiO_2-NRs has about 86% loading of TiO_2 on the CNC surface. The BET specific surface area from nitrogen adsorption–desorption isotherms for CNC/TiO_2-NRs(90) and CNC/TiO_2-NRs(150) was determined to be 66 $m^2\ g^{-1}$ and 13 $m^2\ g^{-1}$, respectively.

To understand and further confirm the phase of the synthesized NRs, powder XRD analysis has been carried out. The XRD patterns of synthesized CNC, CNC/TiO_2-NRs(90) and CNC/TiO_2-NRs(150) are shown in Fig. 2A. The CNC shows its characteristic reflection peaks of cellulose I at 15.4° and 22.6°.[40]

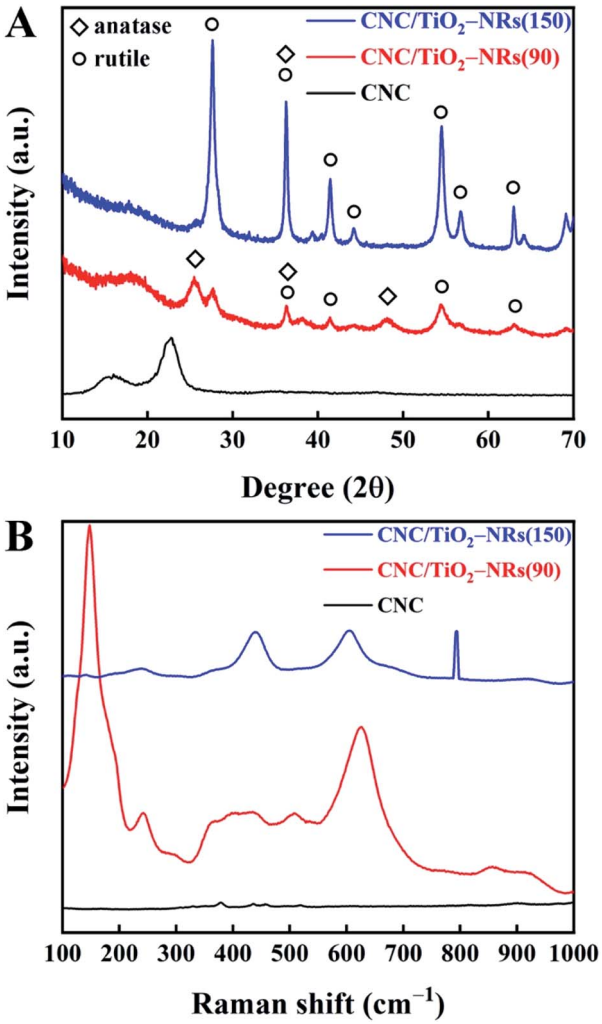

Fig. 2 (A) XRD patterns of CNC, CNC/TiO_2-NRs(90) and CNC/TiO_2-NRs(150) and (B) Raman patterns of CNC, CNC/TiO_2-NRs(90) and CMC/TiO_2-NRs(150).

In the patterns of CNC/TiO_2-NRs(90) and CNC/TiO_2-NRs(150), the characteristic peaks merged into one broad peak at 18.2°. CNC/TiO_2-NRs(90) exhibits predominant peaks at 25.5°, 36.3° and 48.1°, which correspond to the anatase phase (101), (004) and (200) planes (JCPDS 21-1272). Besides, the peaks at 27.7°, 41.4°, 54.5° and 63.0° correspond to rutile phase planes.[47,48] Thus, CNC/TiO_2-NRs(90) sample has a higher degree of the anatase than rutile phases. For the CNC/TiO_2-NRs(150) sample, the reflection peaks at 27.6°, 36.2°, 41.4°, 44.2°, 54.6°, 56.8° and 63.0° represent the corresponding rutile planes (110), (101), (111), (210), (211) (220) and (002) as per JCPDS 21-1276. The intense and well defined peaks suggests that the CNC/TiO_2-NRs(150) sample has a higher degree of crystallinity dominated by the rutile phase.

In addition, the different phases can be further identified in the Raman patterns (Fig. 2B). The existence of metastable anatase can be confirmed with very sharp and intense peak at 147 cm^{-1} (instead of 144 cm^{-1}) and the shoulder at 192 (197) and 624 (635) for CNC/TiO_2-NRs(90). However, CNC/TiO_2-

NRs(150) shows very clear defined peaks at 238 (242), 438 (446) and 604 (610) of the rutile phase.[48]

To overcome the low absorption of TiO_2 in the visible light region, *i.e.* extend the potential photocatalytic performance to the visible region, monodisperse spherical Au NCs were decorated on the CNC/TiO_2-NRs. The mean particle size of the Au NCs before deposition was 8 nm (Fig. S5†). Quantitative analysis performed by inductively coupled plasma optical emission spectrometry (ICP-OES) determined the amount of Au for both samples to be 1.0 wt%. The surface characteristic of the plasmon-enhanced photocatalyst CNC/TiO_2-NRs(150)/Au NCs was studied by electron microscopy. Fig. 3 shows TEM images of CNC/TiO_2-NRs(150)/Au NCs and corresponding elemental maps based on EDS.

The HAADF STEM micrograph in Fig. 3B clearly reveals the deposition of Au NCs with diameter in the range of 8–40 nm. The increased particle size of the Au NCs on the NRs is due to agglomeration of the monodisperse Au NCs. The spatial element distribution was confirmed by EDS mapping (Fig. 3C). The white spots corresponding to Au NCs are distributed along the TiO_2 NRs, which demonstrates the relatively good uniform distribution of Au NCs over the surface of TiO_2 NRs.

The optical properties of CNC/TiO_2-NRs(90) and CNC/TiO_2-NRs(150), without and with Au NCs, were characterized by UV-VIS spectroscopy (Fig. 4). The typical broad absorption peaks are attributed to LSPR in the range 500–600 nm.[49,50] The broadening LSPR peaks originated not only from the broad size distributions of Au NCs (8–40 nm), which has been identified by TEM (*vide supra*), but also from the intercoupling of Au NCs.[51,52] The band gaps of as-prepared materials were estimated with Tauc plots (Fig. S6†), *i.e.* the band gap can be extracted from the $(\alpha h\nu)^{1/n}$ *vs.* $h\nu$ plot intercept.[53,54] The n value for was selected to be 1/2, because the dominating rutile phase in the as-prepared materials is a direct bandgap semiconductor. Furthermore, the Kubelka–Munk function (K–M) was substituted for α in calculation of reflectance from the measured absorbance.[55,56] The band gap of CNC/TiO_2-NRs(90), CNC/TiO_2-NRs(150), CNC/TiO_2-NRs(90)/Au NCs and CNC/TiO_2-NRs(150)/Au NCs is 3.15 eV, 2.98 eV, 3.11 eV and 3.00 eV, respectively. It is clear the decoration of Au NCs can slightly decrease the band gaps of CNC/TiO_2-NRs substrates. Furthermore, the decrement of band gap indicating the improved light absorption toward larger wavelengths. This can result in upsurge of photogenerated electron–hole pairs, since we used AM1.5G illumination, and is beneficial for photocatalytic reactions. We evaluated the solar photocatalytic performance for each sample on RhB degradation.

It is known that H_2O_2 can improve the photocatalytic performance of TiO_2 on dye degradation by inhibiting electron–hole pairs' recombination.[57–59] H_2O_2 not only works as a scavenger of electrons in CB but also helps with the formation of reactive oxygen species, hydroxyl radicals, which are known as a powerful oxidizing agent for organic degradation.[60–62] Therefore, the degradation rate of H_2O_2 on RhB under simulated sunlight was set as a baseline as shown in Fig. 5. Photocatalytic activities of different samples have been studied in the same condition with H_2O_2 with an initial concentration of RhB being equal 8 ppm. The results of the photocatalytic decomposition of

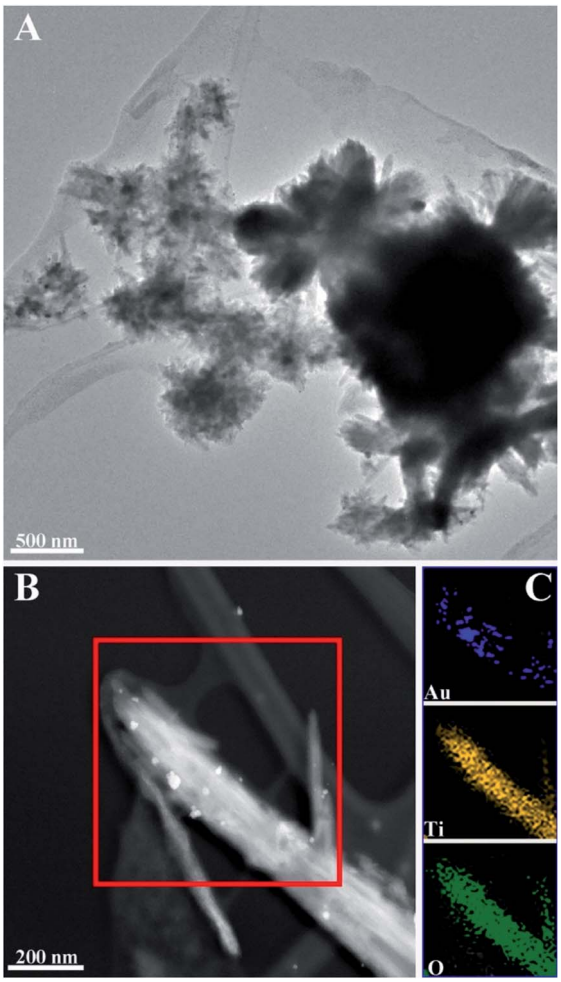

Fig. 3 TEM images of Au NCs deposited TiO_2-NRs(150): (A) morphology of CNC/TiO_2-NRs(150)/Au NCs; (B) HAADF STEM micrograph of TiO_2-NRs(150)/Au NCs and corresponding (C) EDS mapping of Au, Ti and O.

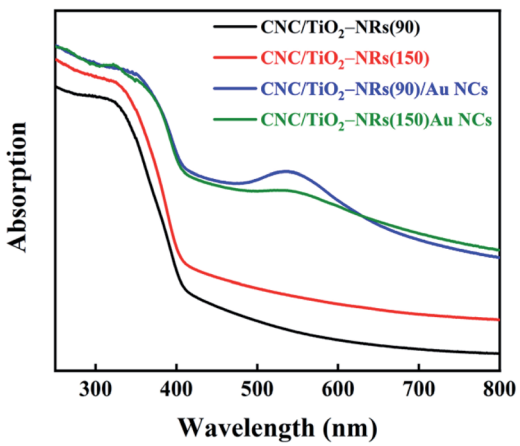

Fig. 4 UV-Vis light absorption spectra of CNC/TiO_2-NRs(90), CNC/TiO_2-NRs(150), CNC/TiO_2-NRs(90)/Au NCs and CNC/TiO_2-NRs(150)/Au NCs.

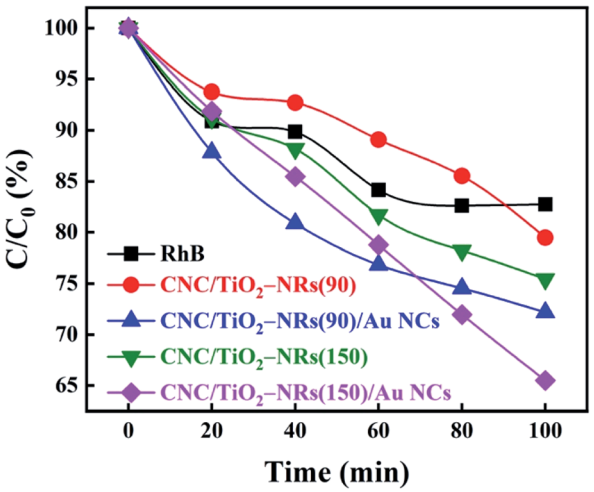

Fig. 5 Photodegradation of RhB (8 ppm in 50 mL of aqueous solution) under simulated sunlight on different photocatalysts (200 mg, powder) supported by H_2O_2. The solution was illuminated with 100 mW cm^{-2} AM 1.5G illumination (1 sun).

RhB indicate that the deposition of Au NCs can ameliorate the photocatalytic performance of both biologic-inorganic hybrid photocatalysts CNC/TiO_2-NRs(90) and CNC/TiO_2-NRs(150). Despite the higher specific surface area, the pristine CNC/TiO_2-NRs(90) sample displayed lower photocatalytic activity than the corresponding CNC/TiO_2-NRs(150) sample. The higher photocatalytic activity of the latter can be explained by the higher temperature of synthesis, which corresponds directly to a lower number of defects and consequently lower charge carrier recombination at defect sites.

To eliminate the interference of dye photosensitization effect on the high dye degradation performance under solar illumination, the decomposition of RhB was compared with CNC/TiO_2-NRs(90) and CNC/TiO_2-NRs(150). Since the Au-functionalized photocatalysts show increased removal efficiency, the LSPR effect plays a key role in the improvement of dye degradation performance on the CNC/TiO_2 photocatalysts. The energy transfer from plasmonic metal to semiconductor in the form of energetic electrons activates O–O bonds and forms reactive oxygen species, allowing the degradation of RhB in our case.[63] The possible mechanisms for the nanostructured plasmon-enhanced CNC/TiO_2-NRs photocatalysts are proposed in Scheme 1. The LSPR effect of Au NCs produces a large number of photogenerated electrons and holes which can participate in the photodegradation process. Although the Au NCs may surely cover also uncoated CNCs, it is the TiO_2/Au interface that can improve meanwhile the charge transfer kinetics.[64]

Conclusions

In summary, the growth of TiO_2 NRs on CNCs retaining the surface functional groups using seed mediated synthesis introduces a new concept of using functionalized substrates to grow inorganic nanostructured photocatalysts. Further modification by using plasmonic NCs augmented the light absorption and thus photocatalytic activity of the CNCs/TiO_2-NRs. Seed mediated synthesis for TiO_2 NRs at 90 °C was demonstrated by using a novel process. The presented method has thus the potential for the production of self-cleaning textiles or wearable dye sensitized solar cells, which were limited up to now to carbon based or high temperature stable substrates. The CNC/TiO_2-NRs structure can serve as template for consecutive functionalization with a second semiconductor. An example are type-II heterojunctions, such as TiO_2/$BiVO_4$, which could further improve charge carrier separation and light absorption in the visible spectra while ensuring fast electronic conductance through titania nanostructures.[65]

Conflicts of interest

There are no conflicts to declare.

Acknowledgements

The authors acknowledge the postdoctoral fellowship (SSN) and financial support (AM) from Wallenberg Wood Science Center. AS acknowledges funding from Vinnova, Sweden's Innovation Agency (project: C1Bio, reference number 2019-03174). We thank Joy Onwumere for fruitful discussion and Tom Willhammar, Istvan-Zoltan Jenei and Cheuk-Wai Tai for help with TEM imaging. Hani Abdelhamid is acknowledged for BET studies. The authors thank Dr Serhiy Budnyk and AC2T research GmbH for ICP analysis within the COMET InTribology (FFG no. 872176, project coordinator: AC2T research GmbH).

Notes and references

1 P. Liu, P. F. Borrell, M. Božič, V. Kokol, K. Oksman and A. P. Mathew, Nanocelluloses and their phosphorylated derivatives for selective adsorption of Ag^{+}, Cu^{2+} and Fe^{3+} from industrial effluents, *J. Hazard. Mater.*, 2015, **294**, 177.
2 H. Voisin, L. Bergström, P. Liu and A. P. Mathew, Nanocellulose-based materials for water purification, *Nanomaterials*, 2017, **7**, 57.
3 T. M. Budnyak, A. Slabon and M. H. Sipponen, Lignin-inorganic interfaces: chemistry and applications from adsorbents to catalysts and energy storage materials, *ChemSusChem*, 2020, **13**, 1.
4 H.-Y. Yu, D.-Z. Zhang, F.-F. Lu and J. Yao, New approach for single-step extraction of carboxylated cellulose nanocrystals for their use as adsorbents and flocculants, *ACS Sustainable Chem. Eng.*, 2016, **4**, 2632–2643.
5 Z. Karim, A. P. Mathew, M. Grahn, J. Mouzon and K. Oksman, Nanoporous membranes with cellulose nanocrystals as functional entity in chitosan: removal of dyes from water, *Carbohydr. Polym.*, 2014, **112**, 668–676.
6 L. Jin, W. Li, Q. Xu and Q. Sun, Amino-functionalized nanocrystalline cellulose as an adsorbent for anionic dyes, *Cellulose*, 2015, **22**, 2443–2456.
7 S. Padalkar, J. R. Capadona, S. J. Rowan, C. Weder, Y.-H. Won, L. A. Stanciu and R. J. Moon, Natural

biopolymers: novel templates for the synthesis of nanostructures, *Langmuir*, 2010, **26**(11), 8497–8502.

8 M. Kaushik and A. Moores, Nanocelluloses as versatile supports for metal nanoparticles and their applications in catalysis, *Green Chem.*, 2016, **18**, 622–637.

9 P. R. Sharma, S. K. Sharma, R. Antoine and B. S. Hsiao, Efficient removal of arsenic using zinc oxide nanocrystal-decorated regenerated microfibrillated cellulose scaffolds, *ACS Sustainable Chem. Eng.*, 2019, **7**, 6140–6151.

10 M.-J. Fang, C.-W. Tsao and Y.-J. Hsu, Semiconductor nanoheterostructures for photoconversion applications, *J. Phys. D: Appl. Phys.*, 2020, **53**, 143001.

11 T. S. Anirudhan and S. R. Rejeena, Photocatalytic degradation of eosin yellow using poly(pyrrole-*co*-aniline)-coated TiO_2/nanocellulose composite under solar light irradiation, *J. Mater.*, 2015, **2015**, 1–11.

12 Q. Zhang, L. Zhang, W. Wu and H. Xiao, Methods and applications of nanocellulose loaded with inorganic nanomaterials: A review, *Carbohydr. Polym.*, 2019, 115454.

13 J. Zeng, S. Liu, J. Cai and L. Zhang, TiO_2 immobilized in cellulose matrix for photocatalytic degradation of phenol under weak UV light irradiation, *J. Phys. Chem. C*, 2010, **114**, 7806–7811.

14 H.-Y. Yu, G.-Y. Chen, Y.-B. Wang and J.-M. Yao, A facile one-pot route for preparing cellulose nanocrystal/zinc oxide nanohybrids with high antibacterial and photocatalytic activity, *Cellulose*, 2015, **22**, 261–273.

15 R. J. Moon, A. Martini, J. Nairn, J. Simonsen and J. Youngblood, Cellulose nanomaterials review: structure, properties and nanocomposites, *Chem. Soc. Rev.*, 2011, **40**, 3941–3994.

16 H. Yano, J. Sugiyama, A. N. Nakagaito, M. Nogi, T. Matsuura, M. Hikita and K. Handa, Optically transparent composites reinforced with networks of bacterial nanofibers, *Adv. Mater.*, 2005, **17**, 153–155.

17 S. S. Nair, J. Forsythe and B. Winther-Jensen, Directing the growth of ZnO nano structures on flexible substrates using low temperature aqueous synthesis, *RSC Adv.*, 2015, **5**, 90881–90887.

18 Y. J. Hwang, A. Boukai and P. Yang, High density n-Si/n-TiO_2 core/shell nanowire arrays with enhanced photoactivity, *Nano Lett.*, 2009, **9**, 410–415.

19 X. Feng, K. Shankar, O. K. Varghese, M. Paulose, T. J. Latempa and C. A. Grimes, Vertically aligned single crystal TiO_2 nanowire arrays grown directly on transparent conducting oxide coated glass: synthesis details and applications, *Nano Lett.*, 2008, **8**, 3781–3786.

20 G. Wang, H. Wang, Y. Ling, Y. Tang, X. Yang, R. C. Fitzmorris, C. Wang, J. Z. Zhang and Y. Li, Hydrogen-treated TiO_2 nanowire arrays for photoelectrochemical water splitting, *Nano Lett.*, 2011, **11**, 3026–3033.

21 B. Tan and Y. Wu, Dye-sensitized solar cells based on anatase TiO_2 nanoparticle/nanowire composites, *J. Phys. Chem. B*, 2006, **110**, 15932–15938.

22 X. Zhang, T. Zhang, J. Ng and D. D. Sun, High-performance multifunctional TiO_2 nanowire ultrafiltration membrane with a hierarchical layer structure for water treatment, *Adv. Funct. Mater.*, 2009, **19**, 3731–3736.

23 B. Liu, H. M. Chen, C. Liu, S. C. Andrews, C. Hahn and P. Yang, Large-scale synthesis of transition-metal-doped TiO_2 nanowires with controllable overpotential, *J. Am. Chem. Soc.*, 2013, **135**, 9995–9998.

24 X. Lv, H. Zhang and H. Chang, Improved photocatalytic activity of highly ordered TiO_2 nanowire arrays for methylene blue degradation, *Mater. Chem. Phys.*, 2012, **136**, 789–795.

25 A. L. Linsebigler, G. Lu and J. T. Yates Jr, Photocatalysis on TiO_2 surfaces: principles, mechanisms, and selected results, *Chem. Rev.*, 1995, **95**, 735–758.

26 A. Fujishima, T. N. Rao and D. A. Tryk, Titanium dioxide photocatalysis, *J. Photochem. Photobiol., C*, 2000, **1**, 1–21.

27 J. Huang, J. Shen, S. Li, J. Cai, S. Wang, Y. Lu, J. He, C. J. Carmalt, I. P. Parkin and Y. Lai, TiO_2 nanotube arrays decorated with Au and Bi_2S_3 nanoparticles for efficient Fe^{3+} ions detection and dye photocatalytic degradation, *J. Mater. Sci. Technol.*, 2020, **39**, 28–38.

28 D. Y. C. Leung, X. Fu, C. Wang, M. Ni, M. K. H. Leung, X. Wang and X. Fu, Hydrogen production over titania-based photocatalysts, *ChemSusChem*, 2010, **3**, 681–694.

29 X. Cheng, Y. Shang, Y. Cui, R. Shi, Y. Zhu and P. Yang, Enhanced photoelectrochemical and photocatalytic properties of anatase-TiO_2 (B) nanobelts decorated with CdS nanoparticles, *Solid State Sci.*, 2020, **99**, 106075.

30 D. B. Ingram and S. Linic, Water splitting on composite plasmonic-metal/semiconductor photoelectrodes: evidence for selective plasmon-induced formation of charge carriers near the semiconductor surface, *J. Am. Chem. Soc.*, 2011, **133**, 5202–5205.

31 A. Gellé and A. Moores, Plasmonic nanoparticles: Photocatalysts with a bright future, *Curr. Opin. Green Sustain. Chem.*, 2019, **15**, 60–66.

32 M. Plodinec, I. Grčić, M. G. Willinger, A. Hammud, X. Huang, I. Panžić and A. Gajović, Black TiO_2 nanotube arrays decorated with Ag nanoparticles for enhanced visible-light photocatalytic oxidation of salicylic acid, *J. Alloys Compd.*, 2019, **776**, 883–896.

33 K.-H. Chen, Y.-C. Pu, K.-D. Chang, Y.-F. Liang, C.-M. Liu, J.-W. Yeh, H.-C. Shih and Y.-J. Hsu, Ag-nanoparticle-decorated SiO_2 nanospheres exhibiting remarkable plasmon-mediated photocatalytic properties, *J. Phys. Chem. C*, 2012, **116**, 19039–19045.

34 E. Hutter and J. H. Fendler, Exploitation of localized surface plasmon resonance, *Adv. Mater.*, 2004, **16**, 1685–1706.

35 C. Clavero, Plasmon-induced hot-electron generation at nanoparticle/metal-oxide interfaces for photovoltaic and photocatalytic devices, *Nat. Photonics*, 2014, **8**, 95.

36 A. Furube, L. Du, K. Hara, R. Katoh and M. Tachiya, Ultrafast plasmon-induced electron transfer from gold nanodots into TiO_2 nanoparticles, *J. Am. Chem. Soc.*, 2007, **129**, 14852–14853.

37 L. Du, A. Furube, K. Yamamoto, K. Hara, R. Katoh and M. Tachiya, Plasmon-induced charge separation and recombination dynamics in gold–TiO_2 nanoparticle

systems: dependence on TiO_2 particle size, *J. Phys. Chem. C*, 2009, **113**, 6454–6462.

38 Z. Zhang and J. T. Yates Jr, Band bending in semiconductors: chemical and physical consequences at surfaces and interfaces, *Chem. Rev.*, 2012, **112**, 5520–5551.

39 Y.-C. Pu, G. Wang, K.-D. Chang, Y. Ling, Y.-K. Lin, B. C. Fitzmorris, C.-M. Liu, X. Lu, Y. Tong and J. Z. Zhang, Au nanostructure-decorated TiO_2 nanowires exhibiting photoactivity across entire UV-visible region for photoelectrochemical water splitting, *Nano Lett.*, 2013, **13**, 3817–3823.

40 D. Bondeson, A. Mathew and K. Oksman, Optimization of the isolation of nanocrystals from microcrystalline cellulose by acid hydrolysis, *Cellulose*, 2006, **13**, 171.

41 S. Camarero Espinosa, T. Kuhnt, E. J. Foster and C. Weder, Isolation of thermally stable cellulose nanocrystals by phosphoric acid hydrolysis, *Biomacromolecules*, 2013, **14**, 1223–1230.

42 A. P. Mathew, K. Oksman, Z. Karim, P. Liu, S. A. Khan and N. Naseri, Process scale up and characterization of wood cellulose nanocrystals hydrolysed using bioethanol pilot plant, *Ind. Crops Prod.*, 2014, **58**, 212–219.

43 M. Davi, T. Schultze, D. Kleinschmidt, F. Schiefer, B. Hahn and A. Slabon, Gold nanocrystal arrays as electrocatalysts for the oxidation of methanol and ethanol, *Z. Naturforsch., B: J. Chem. Sci.*, 2016, **71**, 821–825.

44 R. Zou, Z. Zhang, L. Yu, Q. Tian, Z. Chen and J. Hu, A general approach for the growth of metal oxide nanorod arrays on graphene sheets and their applications, *Chem.–Eur. J.*, 2011, **17**, 13912–13917.

45 W. Guo, F. Zhang, C. Lin and Z. L. Wang, Direct growth of TiO_2 nanosheet arrays on carbon fibers for highly efficient photocatalytic degradation of methyl orange, *Adv. Mater.*, 2012, **24**, 4761–4764.

46 P. Dong, X. Cheng, Z. Huang, Y. Chen, Y. Zhang, X. Nie and X. Zhang, In-situ and phase controllable synthesis of nanocrystalline TiO_2 on flexible cellulose fabrics *via* a simple hydrothermal method, *Mater. Res. Bull.*, 2018, **97**, 89–95.

47 B. Liu and E. S. Aydil, Growth of oriented single-crystalline rutile TiO_2 nanorods on transparent conducting substrates for dye-sensitized solar cells, *J. Am. Chem. Soc.*, 2009, **131**, 3985–3990.

48 H. Cheng, J. Ma, Z. Zhao and L. Qi, Hydrothermal preparation of uniform nanosize rutile and anatase particles, *Chem. Mater.*, 1995, **7**, 663–671.

49 H. Shi, S. Zhang, X. Zhu, Y. Liu, T. Wang, T. Jiang, G. Zhang and H. Duan, Uniform gold-nanoparticle-decorated {001}-faceted anatase TiO_2 nanosheets for enhanced solar-light photocatalytic reactions, *ACS Appl. Mater. Interfaces*, 2017, **9**, 36907–36916.

50 H. Sun, Q. He, P. She, S. Zeng, K. Xu, J. Li, S. Liang and Z. Liu, One-pot synthesis of Au@ material research bulletin TiO_2 yolk–shell nanoparticles with enhanced photocatalytic activity under visible light, *J. Colloid Interface Sci.*, 2017, **505**, 884–891.

51 H. Duan, A. I. Fernández-Domínguez, M. Bosman, S. A. Maier and J. K. Yang, Nanoplasmonics: classical down to the nanometer scale, *Nano Lett.*, 2012, **12**, 1683–1689.

52 H. Hu, H. Duan, J. K. Yang and Z. X. Shen, Plasmon-modulated photoluminescence of individual gold nanostructures, *ACS Nano*, 2012, **6**, 10147–10155.

53 J. Tauc, Absorption edge and internal electric fields in amorphous semiconductors, *Mater. Res. Bull.*, 1970, **5**, 721–729.

54 J. Tauc, R. Grigorovici and A. Vancu, Optical properties and electronic structure of amorphous germanium, *Phys. Status Solidi B*, 1966, **15**, 627–637.

55 A. B. Murphy, Band-gap determination from diffuse reflectance measurements of semiconductor films, and application to photoelectrochemical water-splitting, *Sol. Energy Mater. Sol. Cells*, 2007, **91**, 1326–1337.

56 B. Ohtani, Photocatalysis A to Z—What we know and what we do not know in a scientific sense, *J. Photochem. Photobiol., C*, 2010, **11**, 157–178.

57 J. C. Garcia, J. L. Oliveira, A. E. C. Silva, C. C. Oliveira, J. Nozaki and N. E. De Souza, Comparative study of the degradation of real textile effluents by photocatalytic reactions involving $UV/TiO_2/H_2O_2$ and $UV/Fe^{2+}/H_2O_2$ systems, *J. Hazard. Mater.*, 2007, **147**, 105–110.

58 J. C. Garcia, J. I. Simionato, A. E. C. da Silva, J. Nozaki and N. E. De Souza, Solar photocatalytic degradation of real textile effluents by associated titanium dioxide and hydrogen peroxide, *Sol. Energy*, 2009, **83**, 316–322.

59 D. Wiedmer, E. Sagstuen, K. Welch, H. J. Haugen and H. Tiainen, Oxidative power of aqueous non-irradiated TiO_2–H_2O_2 suspensions: Methylene blue degradation and the role of reactive oxygen species, *Appl. Catal., B*, 2016, **198**, 9–15.

60 A. Syoufian and K. Nakashima, Degradation of methylene blue in aqueous dispersion of hollow titania photocatalyst: study of reaction enhancement by various electron scavengers, *J. Colloid Interface Sci.*, 2008, **317**, 507–512.

61 I. A. Salem, Kinetics and mechanism of the color removal from congo red with hydrogen peroxide catalyzed by supported zirconium oxide, *Transition Met. Chem.*, 2000, **25**, 599–604.

62 Y.-H. Chiu, T.-F. M. Chang, C.-Y. Chen, M. Sone and Y.-J. Hsu, Mechanistic insights into photodegradation of organic dyes using heterostructure photocatalysts, *Catalysts*, 2019, **9**, 430.

63 P. Christopher, H. Xin and S. Linic, Visible-light-enhanced catalytic oxidation reactions on plasmonic silver nanostructures, *Nat. Chem.*, 2011, **3**, 467.

64 Y.-H. Chiu, K.-D. Chang and Y.-J. Hsu, Plasmon-mediated charge dynamics and photoactivity enhancement for Au-decorated ZnO nanocrystals, *J. Mater. Chem. A*, 2018, **6**, 4286–4296.

65 J. Resasco, H. Zhang, N. Kornienko, N. Becknell, H. Lee, J. Guo, A. L. Briseno and P. Yang, $TiO_2/BiVO_4$ nanowire heterostructure photoanodes based on type II band alignment, *ACS Cent. Sci.*, 2016, **2**, 80–88.